













JWST/NIRSpec Observations of Salacia–Actaea and Máni: Exploring Population-level Trends among Water-ice-rich Kuiper Belt Objects

Ian Wong ¹, Bryan J. Holler ¹, Silvia Protopapa ², Aurélie Guilbert-Lepoutre ³, William M. Grundy ^{4,5},
John A. Stansberry ⁶, Heidi B. Hammel ⁷, Stefanie N. Milam ⁸, Rosario Brunetto ⁹, Joshua P. Emery ⁵,
Estela Fernández-Valenzuela ¹⁰ and Noemí Pinilla-Alonso ^{11,12}

¹Space Telescope Science Institute, 3700 San Martin Drive, Baltimore, MD, USA

²Southwest Research Institute, 1301 Walnut Street, Suite 400, Boulder, CO, USA

³LGL-TPE, CNRS, Université Lyon 1, ENSL, Villeurbanne, France

⁴Lowell Observatory, 1400 W Mars Hill Rd., Flagstaff, AZ, USA

⁵Northern Arizona University, Flagstaff, AZ, USA

⁶Space Telescope Science Institute, 3700 San Martin Drive, Baltimore, MD 21218, USA

⁷Association of Universities for Research in Astronomy, Washington, DC, USA

⁸NASA Goddard Space Flight Center, Greenbelt, MD, USA

⁹Université Paris-Saclay, CNRS, Institut d’Astrophysique Spatiale, Orsay

¹⁰Florida Space Institute, University of Central Florida, Orlando, FL, USA

¹¹Institute of Space Science and Technology of Asturias (ICTEA), University of Oviedo, Asturias, Spain

¹²Department of Physics, University of Central Florida, Orlando, FL, USA

Abstract

We present observations of the mid-sized Kuiper belt objects (KBOs) Salacia–Actaea and Máni, obtained with the Near-Infrared Spectrograph on JWST. The satellite Actaea was fully blended with Salacia at the spatial resolution of the integral field unit, and we extracted the combined spectrum. The 0.7–5.1 μm reflectance spectra of Salacia–Actaea and Máni display prominent water-ice absorption bands at 1.5, 2, 3, and 4–5 μm . The ν_3 fundamental vibrational band of carbon dioxide ice at 4.25 μm is present in both spectra. From a quantitative band-depth analysis of the entire current JWST spectroscopic sample of water-ice-rich KBOs, we find strong evidence for a positive covariance between relative water-ice abundance and size, which may indicate the emergent impacts of internal differentiation and cryovolcanic production of surface water ice on mid-sized KBOs. A detailed look at the distribution of 2 and 3 μm band depths suggests additional sources of variability, such as different water-ice grain sizes. In addition, we report an apparent transition in the carbon dioxide band depth at object diameters of roughly 300–500 km, with larger objects showing systematically weaker absorptions, although selection effects within the sample do not allow us to confidently distinguish between a size-dependent phenomenon and a correlation with dynamical class.

United Astronomy Thesaurus concepts: Kuiper belt (893); Trans-Neptunian objects (1705); Surface composition (2115); James Webb Space Telescope (2291)

1. Introduction

Over the past three decades, observational exploration of the Kuiper belt has unveiled an astonishing diversity of surface compositions. While the reflectance spectra of the largest Kuiper belt objects (KBOs) indicate high-albedo surfaces rich in hypervolatile ices (e.g., methane, nitrogen, and carbon monoxide), early observations of smaller KBOs, at wavelengths spanning the visible and near-infrared through 2.5 μm , revealed significantly darker regoliths and mostly featureless spectra, with only water (H₂O) and/or methanol (CH₃OH) ice being robustly detected on a handful of objects (see M. A. Barucci et al. 2008 and M. E. Brown 2012 for high-level reviews of these previous spectroscopic detections). Those results pointed toward a major transition in the surface properties of KBOs separating the largest dwarf planets (e.g., Pluto, Eris, Makemake) from the rest of the population. Volatile loss through atmospheric escape has

been proposed as a first-order explanation for the absence of hypervolatiles on all but the largest KBOs. Without sufficient gravity to sustain a tenuous atmosphere and enable stable gas–solid exchange, highly volatile species such as methane would have been depleted from the surface (e.g., E. L. Schaller & M. E. Brown 2007a; M. E. Brown et al. 2011; S. Protopapa et al. 2025).

While this simple framework successfully accounts for the fundamental distinction between dwarf planets and smaller KBOs, more extensive observations of the Kuiper belt have uncovered additional complexity in its compositional landscape. Recent large-scale photometric surveys (e.g., R. E. Pike et al. 2017; I. Wong & M. E. Brown 2017; P. H. Bernardinelli et al. 2025) and JWST spectroscopic observations (M. N. De Prá et al. 2025; N. Pinilla-Alonso et al. 2025) of KBOs with diameters less than ~ 800 km have identified distinct clusters of objects that differ systematically in their spectral profiles, suggesting the presence of stark composi-

tional gradients within the primordial outer protoplanetary disk among similarly sized planetesimals (e.g., [M. E. Brown et al. 2011](#); [I. Wong & M. E. Brown 2016](#); [C. M. Lisse et al. 2021](#)). It is evident that a more robust understanding of the physical and chemical processes that have shaped the observable properties of KBOs is critical for elucidating the evolutionary trajectories of these distant icy bodies.

Midsized objects, with diameters spanning ~ 800 – 1500 km, are key to disentangling the impacts of size and formation environment on the surface composition of KBOs. The published densities of KBOs in this diameter range, which were measured from the orbital characterization of satellite-hosting systems, display a steep rise with increasing size (e.g., [M. E. Brown 2012](#); [W. B. McKinnon et al. 2017](#); [W. M. Grundy et al. 2019a](#)). Various theories have been put forth to explain this trend, including gravitational collapse of bulk porosity (e.g., [C. J. Bierson & F. Nimmo 2019](#)), size- and location-dependent variations in the accreted rock–ice fraction (e.g., [M. H. Cañas et al. 2024](#)), and large impacts (e.g., [A. C. Barr & M. E. Schwamb 2016](#)). These objects are also an ideal testing ground for probing interior processes such as differentiation, radiogenic heating, and subsurface water–ice melt, which are expected to have a substantial impact on the internal evolution of KBOs at these sizes (see, for example, reviews by [W. B. McKinnon et al. 2008](#) and [A. Guilbert-Lepoutre et al. 2020](#)).

[J. P. Emery et al. \(2024\)](#) present 0.6 – $5\ \mu\text{m}$ JWST observations of three midsized KBOs—Gonggong, Quaoar, and Sedna—which straddle the predicted threshold for methane (CH_4) ice retention from atmospheric volatile loss models (e.g., [E. L. Schaller & M. E. Brown 2007a](#); [J. K. Steckloff et al. 2021](#); [S. Protopapa et al. 2025](#)). The measured spectra are markedly different from both the larger dwarf planets (Pluto, Eris, Makemake) and the smaller KBOs. The most notable feature is the presence of ethane (C_2H_6) ice on all three objects, with Sedna showing additional light hydrocarbon signatures from ethylene and acetylene. Meanwhile, the spectrum of Quaoar yields a clear detection of CH_4 ice, confirming previous findings from ground-based data ([E. L. Schaller & M. E. Brown 2007b](#); [C. M. Dalle Ore et al. 2009](#)).

Given that C_2H_6 and other light hydrocarbons are the immediate byproducts of CH_4 irradiation (e.g., [P. A. Gerakines et al. 2001](#); [C. J. Bennett et al. 2006](#)), and that they in turn readily photolyze into more complex refractory hydrocarbons (e.g., [L. Moroz et al. 2004](#); [C. J. Bennett et al. 2006](#); [E. Quirico et al. 2023](#); [C. Zhang et al. 2023](#)), their persistence on the surfaces of these midsized KBOs likely requires steady replenishment of CH_4 , perhaps from a geochemically sourced reservoir in the interior of these bodies ([C. R. Glein et al. 2024](#); [W. M. Grundy et al. 2024](#); [S. Protopapa et al. 2025](#)), along with a sufficiently long residence time on the surface to allow for radiation processing ([J. P. Emery et al. 2024](#)). These findings suggest that midsized KBOs are not quiescent, primitive bodies, but rather dynamic worlds that manifest both past and possibly ongoing endogenic and exogenic alteration—including internal differentiation, surface–interior exchange, insolation-driven volatile cycling, and space weathering.

In this paper, we present observations of Salacia–Actaea ([H. G. Roe et al. 2005](#); [K. S. Noll et al. 2006](#)) and Máni ([C. A. Trujillo et al. 2002](#))¹ obtained with the Near-Infrared Spectrograph (NIRSpec) on JWST. With radiometric diameters of 901 ± 45 and 934 ± 47 km ([E. Vilenius et al. 2012](#); [S. Fornasier et al. 2013](#); [T. Müller et al. 2020](#)), respectively, these two objects bridge the gap in size between the three mid-sized objects presented in [J. P. Emery et al. \(2024\)](#) and the sample of smaller KBOs characterized in [N. Pinilla-Alonso et al. \(2025\)](#). Hubble imaging of Salacia revealed the binary companion Actaea ([K. S. Noll et al. 2008](#)), which has an orbital period of ~ 5.5 days ([W. M. Grundy et al. 2019b](#)). Using the measured primary–secondary brightness difference of 2.37 ± 0.06 mag ([J. A. Stansberry et al. 2012](#)) and assuming the same albedo, the diameter of Actaea is estimated to be 290 ± 21 km ([M. E. Brown & B. J. Butler 2017](#)). The JWST observations do not resolve the two components of the binary system, and we analyze the combined spectrum. Hereafter, we refer to the Salacia–Actaea system as Salacia, for the sake of brevity.

Despite being among the 10 largest known KBOs, information about the surface properties of Salacia and Máni is relatively scant in the published literature. Ground-based spectroscopy of Salacia showed a moderately red visible color ([N. Pinilla-Alonso et al. 2008](#)) and a featureless near-infrared spectrum from 1.4 to $2.4\ \mu\text{m}$ ([E. L. Schaller & M. E. Brown 2008](#)). Meanwhile, no published spectroscopy of Máni exists; broadband visible photometry of Máni indicated a relatively neutral spectral slope, similar to that of Haumea ([S. C. Tegler et al. 2016](#)). A stellar occultation of Máni revealed a plausibly impact-related topographic depression and an area-equivalent diameter of 796 ± 24 km—significantly smaller than the radiometric measurement, suggesting a possible thermal contribution from an undiscovered dark satellite ([F. L. Rommel et al. 2023](#)). The JWST data described in this work provide the first detailed view of Salacia and Máni at infrared wavelengths.

2. Observations and Data Analysis

Observations of Salacia and Máni were carried out with the integral field unit (IFU) of NIRSpec ([P. Jakobsen et al. 2022](#); [T. Böker et al. 2023](#)) on UT 2022 November 12 and 2022 August 31, respectively, as part of JWST Cycle 1 Guaranteed Time Observations Program #1191 (PI: J. Stansberry). Each observation consisted of a pair of dithered exposures using the low-spectral-resolution double-pass prism, which provides continuous wavelength coverage from 0.6 to $5.3\ \mu\text{m}$ at a spectral resolution of $\Delta\lambda/\lambda = 30$ – 300 . Each exposure had a total integration time of 759 s and utilized the NRSIRS2RAPID readout method, which reduces the effect of detector read noise ([S. H. Moseley et al. 2010](#); [B. J. Rauscher et al. 2012](#)). The heliocentric distance (r_h), distance from JWST (d), and phase angle (α) of Salacia and Máni at the time of the observations were $r_h = 45.1$ au, $d = 44.5$ au, $\alpha = 0^\circ 94$ and $r_h = 46.3$ au, $d = 45.7$ au, $\alpha = 1^\circ 02$, respectively.

¹ Alternate designations: Salacia = 120347 (2004 SB60), Máni = 307261 (2002 MS4).

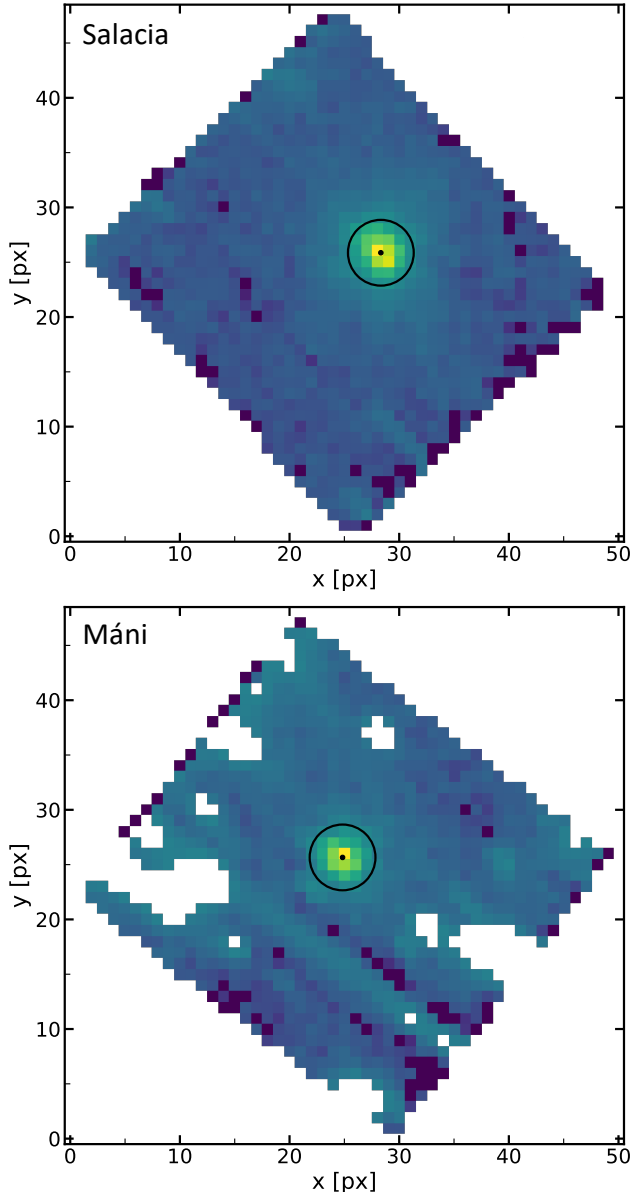


Figure 1. Wavelength-averaged IFU images from the first dithered exposures of Salacia and Máni. A logarithmic stretch was applied to the flux scaling to highlight the PSF shapes and background variations. The black dots and circles denote the best-fit centroid positions and the spectral extraction apertures, respectively. In the case of Máni, the masked pixels across the field of view correspond to relatively bright background sources that were flagged prior to spectral extraction (see text for details).

Starting with the raw uncalibrated detector images downloaded from the Mikulski Archive for Space Telescopes, we used the `jwstspec` pipeline (I. Wong 2025) to generate dark-corrected, flat-fielded, readnoise-corrected, spatially-rectified, and flux-calibrated data cubes for each dithered exposure and carried out optimal spectral extraction; a full description of `jwstspec` and its implementation for spectroscopic observations of solar system small bodies is provided in I. Wong et al. (2025) and references therein. The core of

the data processing workflow is the official JWST calibration pipeline, and the results presented in this paper were derived using Version 1.17.1 (H. Bushouse et al. 2025); all necessary reference files were drawn from context `jwst_1321.pmap` of the JWST Calibration Reference Data System.

Figure 1 shows the wavelength-averaged IFU images from the first dithered exposures of Salacia and Máni. A visual inspection of the point-spread function (PSF) of Salacia reveals a slight deviation from a radially symmetric shape. At the time of the observation, Actaea was $0''.1$ to the northeast of Salacia, according to the JPL Horizons ephemeris, which corresponds to one NIRSpec IFU spatial pixel. It follows that the PSFs of Salacia and Actaea are fully blended in the IFU cubes, and we proceeded to extract both sources together. Assuming the same albedo across the binary pair, the diameter of Actaea is approximately one-third that of Salacia (J. A. Stansberry et al. 2012; M. E. Brown & B. J. Butler 2017), corresponding to $\sim 10\%$ of the total system flux—a negligible contribution to the measured spectrum. In the case of Máni, the target was located in a dense field of background stars. To ensure a reliable measurement of the background flux level, we masked the target and applied an iterative σ -clipping filter to the median image of each data cube to exclude pixels that exceeded the median by more than 3σ .

We calculated the target’s centroid in each data cube from a Gaussian fit to the source PSF and extracted the spectrum using the empirical PSF fitting method within `jwstspec`. Template PSF models were generated for each slice using a 21 pixel wide moving median window along the wavelength axis; these templates were then normalized and fit to the slices with a multiplicative scaling factor to determine the fluxes. Uncertainties were estimated by weighting the pipeline-generated error array of each slice with the corresponding normalized template PSF and computing the quadrature sum of values within the extraction aperture. For both targets, the radius of the spectral extraction aperture was set to 3 pixels, and the background was measured across all unmasked pixels outside of a 21×21 pixel box centered on the target’s centroid. The spectra from the pairs of dithered exposures were passed through a 21 point wide 5σ moving median filter to remove outliers and then averaged using a simple mean to produce the combined irradiance spectrum. The associated uncertainties were obtained through standard error propagation.

To derive the reflectance spectra and account for common-mode instrumental systematics, the irradiance spectrum of each target was divided by the analogously derived spectrum of the solar analog star SNAP-2 (Program #1128; PI: N. Luetzgendorf). To correct for the spectral difference between SNAP-2 and the Sun, we multiplied the reflectance spectrum by the wavelength-dependent ratio between the solar standard spectrum from the Planetary Spectrum Generator (G. L. Villanueva et al. 2018) and the model spectrum of SNAP-2 from CALSPEC (R. C. Bohlin et al. 2014). Figure 2 shows the final normalized reflectance spectra of Salacia and Máni. Both spectra were trimmed to $0.7\text{--}5.1\ \mu\text{m}$ to remove the wavelength regions of low instrument throughput and poor data quality.

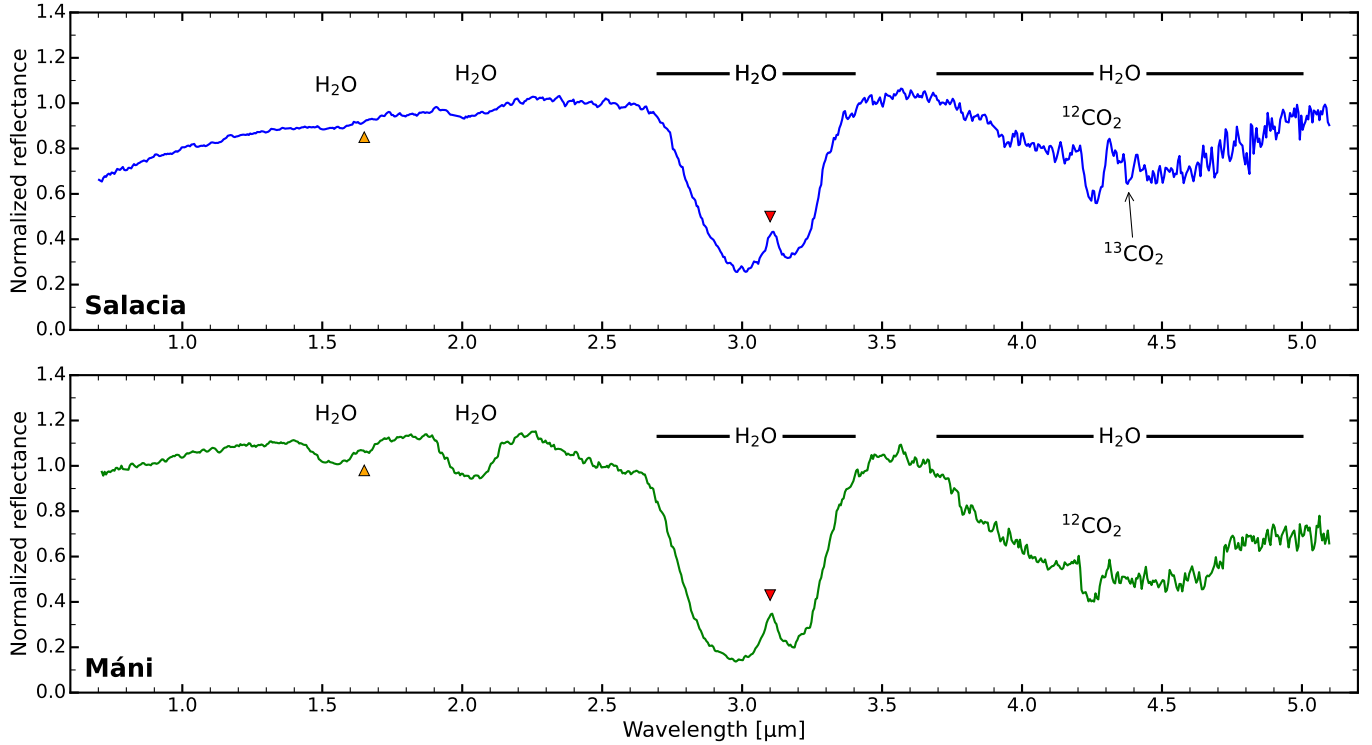


Figure 2. The reflectance spectra of Salacia (top) and Máni (bottom), normalized to unity at $2.5\ \mu\text{m}$. The detected absorption bands of H_2O and CO_2 ice are labeled. The red triangles correspond to the location of the $1.65\ \mu\text{m}$ H_2O -ice spectral feature that likely indicates the crystalline phase, which is clearly discernible in the spectrum of Máni. The inverted orange triangles mark the $3.1\ \mu\text{m}$ Fresnel reflection peak of H_2O ice.

3. Discussion

3.1. Spectral Characterization

The spectra of Salacia and Máni have similar shapes. Both show a deep absorption feature at $3\ \mu\text{m}$, a broad reflectance minimum spanning $4\text{--}5\ \mu\text{m}$, and weaker bands at 1.5 and $2\ \mu\text{m}$ —all of which are the characteristic spectral signatures of H_2O ice. In addition, the two spectra display a sharp Fresnel reflectance peak at $3.1\ \mu\text{m}$ (marked with the red triangles in Figure 2). At $1.65\ \mu\text{m}$, there is a distinct absorption band that, together with the $3.1\ \mu\text{m}$ Fresnel peak, is clearly discernible on Máni (orange triangle); for Salacia, it is difficult to ascertain whether a similar $1.65\ \mu\text{m}$ H_2O -ice feature is present, given the spectrum’s weak $1.5\ \mu\text{m}$ absorption band. Overall, the H_2O -ice features on Máni are significantly stronger than on Salacia across the observed wavelength range, suggesting a higher relative abundance of H_2O on its surface. There are also some differences in the shape of the H_2O -ice features between the two objects: for example, the profile of the broad $4\text{--}5\ \mu\text{m}$ absorption band on Máni has a distinctively sharp rise at around $4.7\ \mu\text{m}$, which is not seen on Salacia. An examination of H_2O -ice optical constants indicates systematic variations in the $4\text{--}5\ \mu\text{m}$ band shape between the crystalline and amorphous phases, with the former showing a somewhat steeper and shorter-wavelength decrease in absorbance across the $4.5\text{--}5.0\ \mu\text{m}$ region (R. M. Mastrapa et al. 2009)—broadly consistent with the observed spectral shape on Máni. It should be noted, however, that variations in H_2O -ice path length as well as surface layering can also contribute to differences in band shapes, relative

band depths, and the presence/absence of the Fresnel peak; proper radiative transfer modeling, which is outside the scope of this paper, is required to fully explore the effects of abundance, grain size, and crystallinity (e.g., G. B. Hansen & T. B. McCord 2004; S. Protopapa et al. 2014, 2021).

At $4.25\ \mu\text{m}$, both Salacia and Máni show a pronounced absorption band attributed to the ν_3 asymmetric stretch mode of solid carbon dioxide (CO_2 ; e.g., P. A. Gerakines & R. L. Hudson 2020). Salacia has an additional narrow feature at $4.37\ \mu\text{m}$ that corresponds to the $^{13}\text{CO}_2$ isotopologue (e.g., J. He et al. 2018). This feature is not apparent on Máni, although we note that the typical signal-to-noise ratio of the spectra in this region is relatively low compared to shorter wavelengths, which makes the detection of weak, narrow features such as the $^{13}\text{CO}_2$ band very challenging. Indeed, the overall scatter in measured reflectance for Salacia across $4.3\text{--}4.7\ \mu\text{m}$ is comparable to the observed depth of the $^{13}\text{CO}_2$ feature. Future JWST observations with significantly longer exposure times are needed to precisely measure the $^{13}\text{C}/^{12}\text{C}$ ratio in CO_2 ice on KBOs and probe for trends across the population.

Spectroscopic observations of dozens of smaller KBOs obtained with NIRSpec during the first year of JWST science operation have revealed three compositional classes (M. N. De Prá et al. 2025; J. Licandro et al. 2025; N. Pinilla-Alonso et al. 2025): (1) a subpopulation with moderately red visible colors that displays strong H_2O -ice absorption bands and weaker CO_2 -ice features; (2) a class with systematically redder colors and deep CO_2 -ice features that also exhibits prominent absorptions from solid carbon monoxide and en-

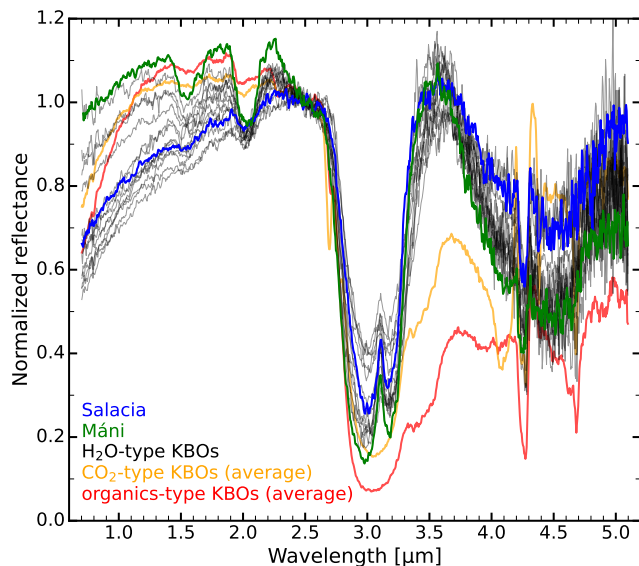


Figure 3. The reflectance spectra of Salacia (blue) and Máni (green) alongside the sample of H₂O-type KBOs (black) from [N. Pinilla-Alonso et al. \(2025\)](#), illustrating the broad similarities in overall continuum shape and absorption bands. The average CO₂-type KBO (orange) and organics-type KBO (red) spectra are also included for comparison. All spectra have been normalized to unity at 2.5 μm .

hanced signatures of irradiated aliphatic organics; (3) a separate group of objects with even redder average visible colors that display a negative-sloped near-infrared continuum and much stronger organic features, along with the diagnostic spectral bands of CH₃OH ice. Members of the Haumea collisional family are considered a separate group of exceptionally water-ice-rich KBOs and are not included as part of the three compositional classes delineated here. Recently, [B. J. Holler et al. \(2025\)](#) proposed a new taxonomic nomenclature for these three compositional classes—spectrally prominent water (H₂O-type), spectrally prominent carbon oxides (CO₂-type), and spectrally prominent organics (organics-type)—which we adopt in this paper. These classes have previously been referred to, respectively, as “bowl”-, “double-dip”-, and “cliff”-type in the literature (e.g., [N. Pinilla-Alonso et al. 2025](#)).

Visual comparisons of Salacia and Máni with the three compositional classes show that their spectra align most closely with the H₂O-type KBOs. In Figure 3, the spectra of Salacia and Máni are plotted against the set of individual spectra of H₂O-type KBOs from [N. Pinilla-Alonso et al. \(2025\)](#), along with the average spectra of the CO₂-type and organics-type KBOs. All of the H₂O-type KBO spectra exhibit the same prominent H₂O and CO₂ absorption bands and overall spectral profile as Salacia and Máni. Meanwhile, the CO₂- and organics-type spectra have drastically different continuum shapes and distinct collections of absorption features; most notably, both CO₂- and organics-type KBOs show strong aliphatic organics signatures at 3.3–3.6 μm (e.g., [R. Brunetto et al. 2006](#)), which are not seen on Salacia, Máni, or any of the other H₂O-type KBOs.

The stark spectral differences between the aforementioned three compositional classes suggest distinct formation locations in the outer solar system. Several previous works have hypothesized the existence of steep compositional gradients within the primordial trans-Neptunian planetesimal disk, driven by differential volatile retention as a function of heliocentric distance (e.g., [M. E. Brown et al. 2011](#); [I. Wong & M. E. Brown 2016](#); [C. M. Lisse et al. 2021](#)). It follows that the H₂O-type KBOs, which show the fewest volatile ice signatures, would have formed closest to the inner edge of this disk ([N. Pinilla-Alonso et al. 2025](#)). Within this explanatory framework, Salacia and Máni can be classified as two of the largest members of the broader H₂O-type class that all shared a common formation environment and were subsequently scattered throughout the Kuiper belt during the dynamical instability (e.g., [H. F. Levison et al. 2008](#); [D. Nesvorný 2018](#)).

Notably, the nondetection of the diagnostic spectral signatures of simple hydrocarbons (e.g., CH₄ and C₂H₆) and the absence of the broad 3.3–3.6 μm absorption band due to aliphatic organics on Salacia and Máni mark a critical distinction with Gonggong, Quaoar, and Sedna ([J. P. Emery et al. 2024](#)), which are only slightly larger than Salacia and Máni, with radiometric diameters of 1230 ± 50 km ([C. Kiss et al. 2019](#)), 1074 ± 38 km ([S. Fornasier et al. 2013](#)), and 995 ± 80 km ([A. Pál et al. 2012](#)), respectively. One possible explanation for this discrepancy is that the smaller size and consequently weaker surface gravity of Salacia and Máni do not allow for a sufficiently long retention time of CH₄ ice to enable the production of longer-chain hydrocarbons through radiolysis or photolysis. To explore this line of reasoning more quantitatively, we consider the escape velocities of mid-sized KBOs. For Salacia, Quaoar, and Gonggong, which have masses constrained by observations of their satellites (e.g., [W. M. Grundy et al. 2019b](#); [C. Kiss et al. 2019](#); [C. Collyer et al. 2025](#); [B. Proudfoot et al. 2025](#)), the escape velocities are 385, 542, and 616 m s^{-1} , respectively. The speed of a CH₄ molecule desorbed from a surface with a temperature of 30–50 K is governed by the Armand distribution (e.g., [G. Armand 1977](#)), which peaks at lower velocities in the 200–300 m s^{-1} range. Only the most rapidly moving molecules in the tail of the Armand distribution have sufficient momentum to escape. The difference between escape velocities of 385 and 542 m s^{-1} translates to a roughly order of magnitude larger fraction of desorbed CH₄ molecules that exceed the escape velocity on Salacia than on Quaoar.

It follows that a CH₄ molecule on Quaoar’s surface undergoes an order of magnitude more ballistic hops before escaping. This greatly increases the probability that a CH₄ molecule encounters a cold trap (e.g., the winter hemisphere of a high-obliquity object), where it is stable to sublimation loss. [W. M. Grundy et al. \(2016\)](#) and [U. Raut et al. \(2022\)](#) demonstrated that resonantly scattered Ly α photons can strike the nonilluminated hemispheres of KBOs in sufficient quantities to effectuate irradiation processing of cold-trapped CH₄ into heavier, less volatile hydrocarbons (e.g., C₂H₆). The situation is more uncertain for Máni and Sedna, which are very close in size but have no dynamical mass measurements. If we take their radiometric diameters and as-

sume the same bulk density as Salacia— 1.50 g cm^{-3} (W. M. Grundy et al. 2019b)—we obtain comparable escape velocities of 430 and 460 m s^{-1} , respectively. However, Sedna’s distant aphelion entails lower surface temperatures than the other mid-sized KBOs, which consequently augment its ability to retain CH_4 and produce the light hydrocarbon signatures seen in its spectrum.

It is also possible that the absence of C_2H_6 or other light hydrocarbons is due to a much lower inherent abundance of CH_4 on Salacia and Máni than on Gonggong, Quaoar, and Sedna. In light of the proposed geochemical origin of endogenically sourced CH_4 on the dwarf planets Eris and Make-make (C. R. Glein et al. 2024; W. M. Grundy et al. 2024), the absence of CH_4 and its associated irradiation products may indicate that Salacia and Máni do not have the requisite physical conditions in their interiors to support the thermogenic production of CH_4 and its transport to the surface. Alternatively, based on the previously discussed explanatory framework for the three KBO compositional classes, the broad similarity between Salacia, Máni, and the H_2O -type KBOs suggests that they formed in the innermost region of the primordial trans-Neptunian disk, where the higher temperatures led to rapid depletion of CH_4 ice on the surfaces of planetesimals, thereby curtailing the formation of hydrocarbons and more complex refractory organics that could be incorporated into the resultant bodies.

3.2. Trends in Absorption Band Depths

The ensemble of H_2O -type KBO spectra in Figure 3 spans a broad range of relative band depths and continuum slopes. In fact, regardless of the choice of normalization wavelength, these spectra exhibit a significantly larger dispersion in spectral shape than the PO- and CO_2 -type compositional classes, indicating a particularly high level of compositional diversity within the H_2O -type class. This finding motivated us to examine the variations in spectral properties among H_2O -type KBOs in a more quantitative manner.

We carried out a systematic band-depth analysis of the strongest H_2O and CO_2 features at 2 , 3 , and $\sim 4.25 \mu\text{m}$. The spectroscopic sample was expanded to include other H_2O -type targets that were observed with NIRSpc: (a) six Neptune Trojans that were published in L. Markwardt et al. (2025), (b) four Centaurs from J. Licandro et al. (2025), (c) three extreme trans-Neptunian objects (ETNOs) with distant perihelia observed as part of Cycle 3 Program #4665 (Holler et al. 2025, in preparation), (d) the blue binary cold classical KBO 2016 BP81 (I. Wong et al. 2025), (e) the mid-sized objects Orcus and Achlys, from Cycle 1 Guaranteed Time Observations Program #1231, and (f) Charon, which was presented in S. Protopapa et al. (2024). The full sample includes 33 objects. All spectra were extracted using an analogous procedure to the one applied to Salacia and Máni (Section 2). When computing the band depths and associated uncertainties, we followed the methodology described in I. Wong et al. (2025); the same continuum and band center regions were used, with the exception of the CO_2 fundamental band near $4.25 \mu\text{m}$. For some of the largest objects—namely, Orcus, Máni, and Achlys—the location of minimum reflectance is shifted toward shorter wavelengths, and we correspondingly

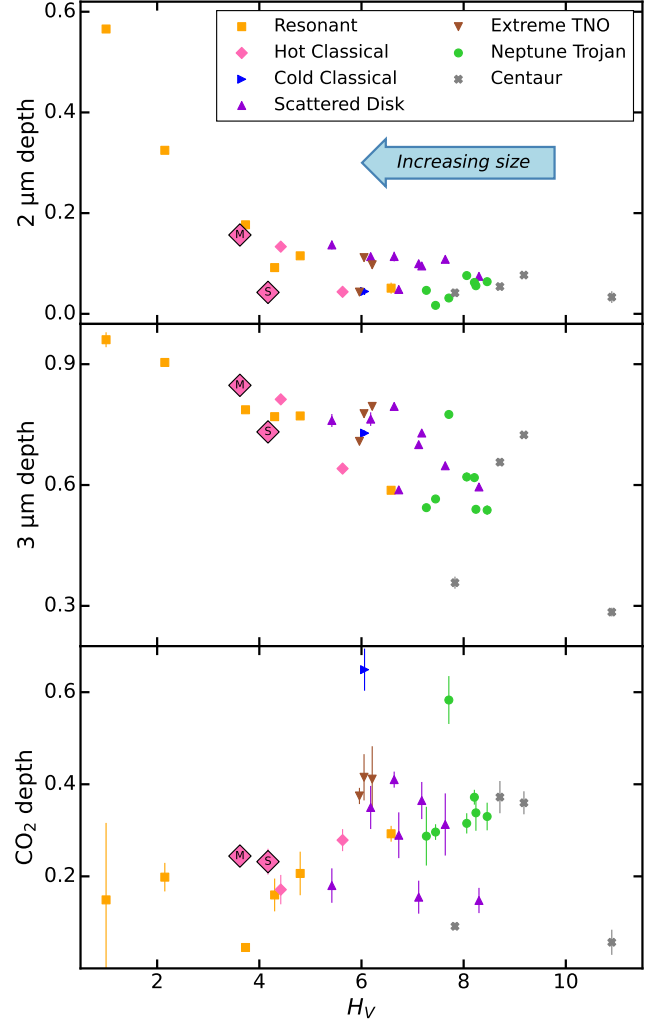


Figure 4. Plot of the measured band depths of the $2 \mu\text{m}$ H_2O (top), $3 \mu\text{m}$ H_2O (middle), and $\sim 4.25 \mu\text{m}$ fundamental CO_2 absorption features as a function of V-band absolute magnitude H_V for H_2O -type objects. The points are color coded by dynamical class. The band depths for Salacia and Máni are highlighted by the larger markers and labeled “S” and “M,” respectively. The three brightest/largest H_2O -type members of the resonant KBO population (orange squares) are, in order, Charon, Orcus, and Achlys. The band-depth values, absolute magnitudes, and dynamical classifications shown in this figure are available as a machine-readable data behind the figure file.

altered the designated band center region from $4.26\text{--}4.28 \mu\text{m}$ to $4.24\text{--}4.26 \mu\text{m}$ when calculating the CO_2 band depth for those three objects. The implications of this spectral behavior are discussed in the following subsection.

In Figure 4, the measured 2 , $3 \mu\text{m}$, and CO_2 fundamental band depths for the H_2O -type KBOs are plotted against V-band absolute magnitude (H_V), which we use here as a proxy for size; the H_V values were sourced from JPL Horizons. The objects are color coded to denote their respective dynamical classifications, as tabulated in K. Volk & C. Van Laerhoven (2024). Salacia and Máni are labeled with “S” and “M,” respectively. There are clear selection effects in

the dataset with respect to object brightness—the Neptune Trojans and Centaurs sample systematically higher H_V values (i.e., smaller sizes) due to their smaller heliocentric distances, while the largest and brightest objects are exclusively from the resonant and hot classical KBO populations. However, when assessing the band-depth distribution of objects with similar H_V values, no significant correlations with dynamical class are apparent.

3.2.1. Water Ice

The depth of the $2\text{ }\mu\text{m}$ H₂O-ice absorption feature decreases with increasing H_V , indicating that smaller/fainter objects tend to show weaker H₂O-ice spectral signatures. The relative positions of Salacia and Máni in the top panel of Figure 4 are readily validated by a visual comparison of their reflectance spectra (Figure 2). To assess the statistical significance of the depth versus H_V trend across the full sample, we computed the Pearson correlation coefficient and obtained $r = -0.72$ with a p -value of 1.4×10^{-6} , indicating that the correlation is statistically significant at the 4.7σ level. However, the strength of the overall correlation is primarily driven by the largest objects with $H_V \lesssim 5$, where the $2\text{ }\mu\text{m}$ depth decreases steeply with increasing H_V ($r = -0.95$, 3.6σ). Among smaller objects, the covariance is weaker and less statistically significant ($r = -0.35$, 1.7σ). This behavior was previously reported based on analyses of ground-based spectra (e.g., M. A. Barucci et al. 2011; M. E. Brown et al. 2012), although the precision of those band-depth measurements for objects with $H_V \gtrsim 4$ was severely limited by the quality of the data. Moreover, almost all of the objects with $H_V \gtrsim 6$ in the extant spectroscopic sample at that time were Centaurs, which may have experienced a divergent surface evolution from the KBO population due to their smaller heliocentric distances. As such, the relationship between band depth and size among KBOs with $H_V \gtrsim 4$ was uncertain.

The exquisite precision of the JWST spectra has provided a detailed view of the $2\text{ }\mu\text{m}$ band-depth distribution through $H_V = 8$. Notably, there is strong evidence for a bifurcation in the measured $2\text{ }\mu\text{m}$ band depths, particularly within the range $4 < H_V < 8$. Two subgroups are identified: one with near-zero band depths (including Salacia) that shows no clear correlation with H_V and another with systematically deeper absorption features that exhibits a modest decrease in depth with increasing H_V . Applying Hartigan’s dip test (J. A. Hartigan & P. M. Hartigan 1985) yields a 3.3σ detection of bimodality.

The broad near-infrared wavelength coverage provided by JWST has uncovered, for the first time, a robust size-dependent trend in the $3\text{ }\mu\text{m}$ H₂O absorption band. The $3\text{ }\mu\text{m}$ band depth decreases monotonically with increasing H_V across the sample of H₂O-type KBOs ($r = -0.82$, 5.4σ). Moreover, we find statistically significant correlations within individual dynamical classes that span more than 2 mag in H_V , specifically resonant objects, hot classicals, and scattered disk objects. This suggests that the relationship between $3\text{ }\mu\text{m}$ band depth and size is not confined to particular regions of the Kuiper belt but is instead a general feature of the population at large.

The distinctive steepening of the $2\text{ }\mu\text{m}$ band-depth trend at the smallest H_V values is not mirrored in the $3\text{ }\mu\text{m}$ band depths. This can be attributed to the onset of saturation, with the two largest KBOs in the sample—Charon and Orcus—having $3\text{ }\mu\text{m}$ band depths in excess of 90%. Meanwhile, two Centaurs—Okyrhoe and 2010 KR59—have exceptionally shallow $3\text{ }\mu\text{m}$ absorptions. This behavior, which is discussed in detail in J. Licandro et al. (2025), may stem from the effects of secondary evolutionary processes that have altered the surfaces of these Centaurs following their migration into the warmer giant planet region. Thermal processes, such as devolatilization and the formation of ice-poor lag deposits resulting from cometary activity, provide plausible explanations for the observed attenuation of the $3\text{ }\mu\text{m}$ H₂O-ice absorption feature. Due to the possibly evolved nature of Centaurs, we do not consider them in the following discussion.

Notably, unlike in the case of the $2\text{ }\mu\text{m}$ band depths, no apparent bifurcation is apparent in the $3\text{ }\mu\text{m}$ band depths across the range $4 < H_V < 8$. This contrast may arise from variations in the extinction coefficient of H₂O ice, which is much smaller at $2\text{ }\mu\text{m}$ than at $3\text{ }\mu\text{m}$. Consequently, the penetration depth of reflected sunlight into the surface is more than an order of magnitude greater at $2\text{ }\mu\text{m}$ (e.g., S. Protopapa et al. 2024). The observed bimodality in the $2\text{ }\mu\text{m}$ band depth among the H₂O-type objects could therefore be indicative of a marked difference in H₂O-ice grain sizes below the outermost surface layer.

If we assume that the $3\text{ }\mu\text{m}$ band depth serves as a proxy for H₂O-ice abundance, the overall trend in the $3\text{ }\mu\text{m}$ band depths is consistent with a steady increase in relative surface H₂O-ice abundance with increasing size. There is, however, considerable scatter in the band-depth distribution, particularly at $H_V > 6$. The significant spread in measured depths among similarly sized objects may be attributed to variations in H₂O-ice grain size across the H₂O-type population. Taken together, the behavior of the 2 and $3\text{ }\mu\text{m}$ H₂O-ice absorption features may indicate some level of vertical stratification on the surfaces of these objects. Detailed spectral modeling of the full spectroscopic ensemble is necessary to retrieve reliable information about the exact physical configuration of H₂O ice on these bodies and disentangle the effects of abundance, grain size, and layering on the observed spectra.

Both radioactive decay and the onset of internal differentiation are exothermic processes whose impacts strongly scale with increasing size (see review by A. Guilbert-Lepoutre et al. 2020). Theoretical modeling has demonstrated that differentiation of ice-rich planetesimals can begin to occur at diameters above ~ 500 km (e.g., H. Hussmann et al. 2006; W. B. McKinnon et al. 2008; U. Malamud & D. Prialnik 2015), which corresponds to $H_V \sim 4.7$, assuming a geometric albedo of 0.1. As seen in Figure 4, this brightness level roughly matches the location below which the 2 and $3\text{ }\mu\text{m}$ H₂O-ice band depths rise most dramatically. Radiogenic heating due to the decay of long-lived isotopes may also be enhanced in large- and mid-sized KBOs above ~ 500 – 1000 km in diameter, which have systematically higher bulk densities and plausibly higher rock–ice fractions (e.g., M. E. Brown 2012; W. B. McKinnon et al. 2017). The internal heating from these processes likely caused widespread melting

and mobilization of H₂O in the interiors of the largest KBOs and may have sustained subsurface liquid water oceans for a significant fraction of the age of the solar system (e.g., H. Hussmann et al. 2006; W. B. McKinnon et al. 2008; S. J. Desch et al. 2009). Cryovolcanic activity could have facilitated the advection of liquid water onto the exterior (e.g., J. C. Cook et al. 2007; S. J. Desch et al. 2009; A. Delsanti et al. 2010; S. M. Menten et al. 2022), thereby enriching the surface with H₂O ice and producing the observed positive correlation between relative H₂O-ice abundance and size. Large-scale cryovolcanism has been proposed to explain the compositional and geological diversity on the surfaces of Pluto and Charon revealed by *New Horizons* (see review by J. M. Moore & W. B. McKinnon 2021 and references therein).

If the observed covariances between H₂O-ice band depths and H_V are indicative of an enrichment of H₂O ice on the surfaces of the largest objects, we expect to find corresponding size-modulated variability in both surface color and albedo. The reflectance spectrum of H₂O ice has a distinctively negative-sloped continuum across the 0.5–2.5 μm range (e.g., W. M. Grundy & B. Schmitt 1998; S. G. Warren & R. E. Brandt 2008; R. M. E. Mastrapa et al. 2013); an enhancement in relative surface H₂O-ice fraction should therefore manifest as a bluing of the spectral slope. Likewise, a higher surface ice fraction should entail an elevated visible geometric albedo. As illustrated in Figure 3, the H₂O-type KBOs span a wide range of near-infrared continuum slopes. We renormalized all of the reflectance spectra in our sample to unity at 1.0 μm and fit a linear slope across 0.7–1.0 μm . While most of the measured slope values do not exhibit a correlation with H_V or 2 μm H₂O-ice band depth, the four largest objects (Charon, Orcus, Achlys, and M \acute{a} ni) have systematically shallower (e.g., more neutral) continua than the rest of the sample. Similarly, we assessed the distribution of radiometrically measured albedo values across the H₂O-type sample (taken from the compilation in N. Pinilla-Alonso et al. 2025 and references therein). While typical albedos (including those of Salacia and M \acute{a} ni) lie between 0.04 and 0.13, the two largest objects are significantly more reflective. Orcus has a measured albedo of 0.231 ± 0.018 (S. Fornasier et al. 2013); *New Horizons* mapping of Charon’s surface yielded albedos in the range 0.20–0.73 (B. J. Buratti et al. 2017). These findings offer strong support to the idea of systematic surface H₂O-ice enrichment on the largest H₂O-type KBOs.

3.2.2. Carbon Dioxide Ice

Turning our attention now to CO₂ (bottom panel of Figure 4), we find two objects—the cold classical binary 2016 BP81 and the Neptune Trojan 2011 SO277—with significantly larger ~ 4.25 μm band depths than the rest of the sample. The distinct spectral behavior of these two outliers was previously reported by I. Wong et al. (2025), who posited that the unique characteristics may reflect in situ formation of blue binaries within the cold classical region during the earliest stages of the protoplanetary disk, under markedly different thermophysical conditions than objects that accreted later (D. Nesvorný et al. 2022). The subsequent orbital restructuring of the Kuiper belt would then have scattered a fraction of these objects into different dynamical populations, thereby

explaining the distinctive spectral shape of 2011 SO277 relative to the other Neptune Trojans in the sample.

Excluding the two objects with exceptionally deep CO₂-ice features (as well as the Centaurs), we find strong evidence for a transition in the average CO₂-ice band depth at around $H_V \sim 5-6$, with the larger KBOs displaying systematically weaker CO₂ absorptions than the smaller objects. When applying the two-sample Kolmogorov–Smirnov test to the CO₂ band-depth distributions on either side of $H_V = 5.5$, we found that they differ at the 4.2σ level. Meanwhile, there is no evidence for correlations with H_V on either side of the threshold ($|r| < 0.15$). Considering the selection biases among the various dynamical classes within the spectroscopic sample, it is not possible to firmly distinguish between an overall trend with size (as in the case of the H₂O-ice absorption features) and a dependency on dynamical class. It is worth noting that, while the resonant objects, hot classicals, Neptune Trojans, and ETNOs appear to cluster within the space of measured CO₂ band depths, the scattered disk objects span a much broader range of values. Additional observations of H₂O-type KBOs that expand the spectroscopic sample within the various dynamical classes to a wider range of sizes are needed to definitively resolve this ambiguity in the nature of the observed CO₂ band-depth behavior.

While it may be tempting to attribute the observed transition in CO₂ band depth to a systematic difference in relative CO₂-ice abundance, a recent compositional analysis of Charon’s JWST spectrum has highlighted the complexities inherent in interpreting CO₂-ice features in spectra dominated by H₂O-ice (S. Protopapa et al. 2024). Charon’s high-resolution spectrum ($\Delta\lambda/\lambda \sim 2700$) reveals the narrow $\nu_1 + \nu_3$ combination band at 2.7 μm in addition to the ν_3 fundamental at ~ 4.25 μm , enabling more robust characterization of the physical nature of CO₂. In that study, the position and shape of the $\nu_1 + \nu_3$ combination band at 2.7 μm were attributed with high confidence to crystalline CO₂ segregated from H₂O, while the form of the ~ 4.25 μm fundamental band was attributed to a two-layer structure in which amorphous H₂O ice and crystalline CO₂ particles overlie a substrate of crystalline H₂O ice and tholin-like material. An interplay between endogenous and exogenous sources of CO₂ was invoked, with the preferred explanation involving subsurface CO₂ exposed by cratering events (S. Protopapa et al. 2024). For the other objects in our H₂O-type KBO sample, the CO₂ combination band at 2.7 μm would be greatly attenuated at the low resolution ($\Delta\lambda/\lambda \sim 100$) of the spectra. To roughly quantify the detectability of this feature on Salacia and M \acute{a} ni, we fit the 2.6–2.8 μm continuum with a cubic spline and constrained the relative magnitude of reflectance deviations near 2.7 μm to at most a few percent.

A close inspection of the CO₂ feature across the ensemble of H₂O-type KBO spectra reveals a notable variation in the ~ 4.25 μm band shape. Figure 5 plots a selection of spectra for objects with a range of H_V values. While the relatively small objects show a characteristic V-shaped absorption feature with a minimum near 4.27 μm —consistent with pure crystalline CO₂ ice (e.g., P. A. Gerakines & R. L. Hudson 2020) or H₂O:CO₂ mixtures (e.g., S. Protopapa et al. 2024; M. N. De Prá et al. 2025)—the larger KBOs display

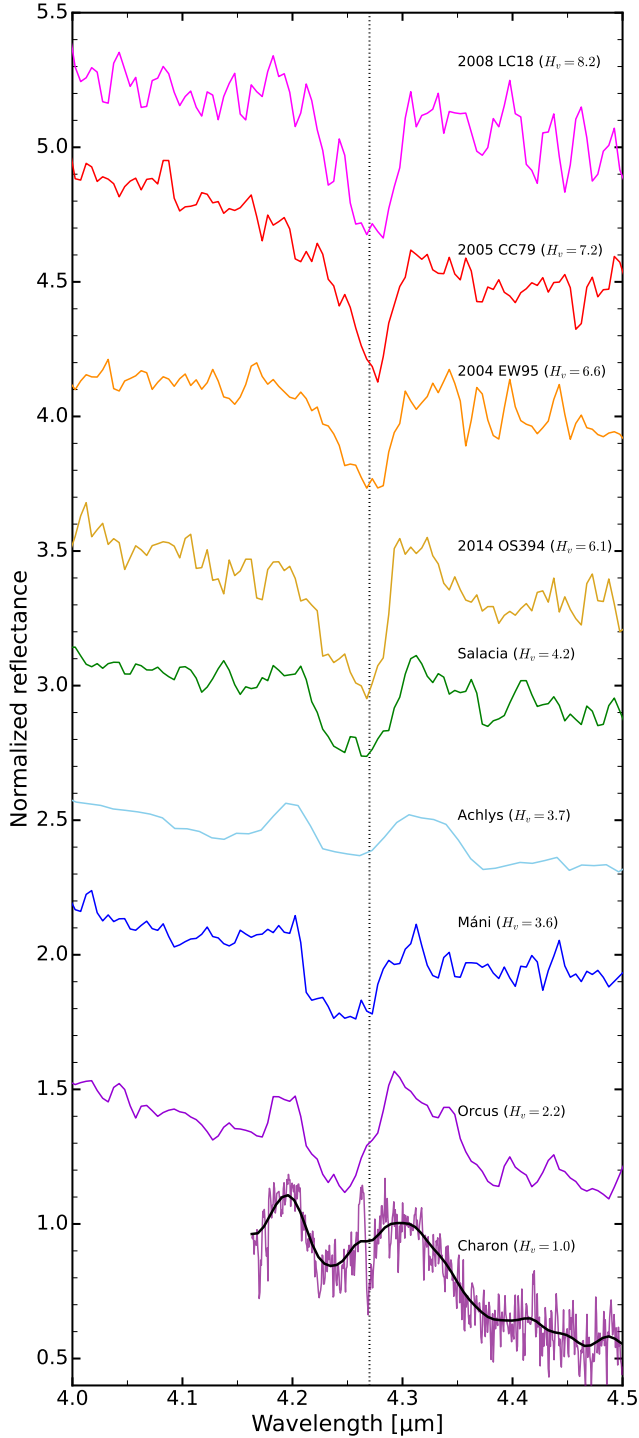


Figure 5. A selection of 4.0–4.5 μm reflectance spectra of H_2O -type KBOs, normalized to unity at 4.3 μm . The spectra are arranged from top to bottom in order of increasing object size. The vertical dotted line at 4.27 μm denotes the expected band center for crystalline CO_2 ice. The larger objects display distinctly broader and blue-shifted absorption features than the smaller KBOs. The spectrum of Charon, obtained with the high-spectral-resolution G395H grating of NIRSPEC, reveals complex fine structure within the CO_2 band. The black curve shows the same spectrum convolved to the lower spectral resolution of the PRISM grating.

broader signatures with flatter reflectance minima that extend to shorter wavelengths. The CO_2 feature in the spectrum of Charon, obtained at a significantly higher spectral resolution, exhibits a unique double-peaked absorption profile, with two minima separated by a reflectance peak at 4.265 μm . Comparisons with the JWST spectrum of Europa, which presents a similar although not identical double-lobed absorption band (S. K. Trumbo & M. E. Brown 2023; G. L. Villanueva et al. 2023), together with laboratory spectra of CO_2 ice preirradiation and postirradiation in both pure and mixed configurations, have enabled investigation into whether Charon’s distinctive CO_2 band structure is due to separate contributions from pure crystalline CO_2 ice and CO_2 embedded in a complex H_2O /organic-rich molecular environment (S. Protopapa et al. 2024). An alternative explanation, which was favored by the authors and motivated by the layered configuration containing a fine-grained upper layer of CO_2 ice, posits that the apparent double-peaked structure is caused by a Fresnel peak of CO_2 ice (S. Protopapa et al. 2024).

Looking farther afield to other small body populations, we find numerous examples of blue-shifted CO_2 fundamental absorption bands among the Jovian and Saturnian moons, including Callisto, Ganymede, Iapetus, Phoebe, and several irregular satellites (C. A. Hibbitts et al. 2000, 2003; D. P. Cruikshank et al. 2010; N. Pinilla-Alonso et al. 2011; D. Bockelée-Morvan et al. 2024; R. J. Cartwright et al. 2024; M. Belyakov & M. E. Brown 2025; B. N. L. Sharkey et al. 2025). A similar 4.25 μm CO_2 feature is also seen on Eurybates—a collisional family member within the Jupiter Trojans (I. Wong et al. 2024). Due to the higher surface temperatures of these middle solar system bodies, pure CO_2 ice is unstable and must therefore be present in more refractory configurations, e.g., H_2O – CO_2 mixtures, mineral-bound CO_2 , or irradiation-produced carbonic acid (e.g., C. A. Hibbitts et al. 2003; B. M. Jones et al. 2014; L. Schiltz et al. 2024).

The limitations in the resolving power and signal-to-noise ratio in the sample of KBO spectra obtained with the prism prevent us from being able to make definitive statements about the nature of CO_2 ice on these bodies. Convolving the spectrum of Charon to the same resolving power as the other spectra largely obscures the fine structure, as illustrated by the solid black curve in Figure 5. Moreover, as mentioned previously, we do not detect CO_2 overtone bands around 2.7 μm , which have been shown to be highly diagnostic of the particular configuration of CO_2 on the surface—whether the CO_2 is in a pure state (e.g., U. Raut & R. A. Baragiola 2013; P. A. Gerakines & R. L. Hudson 2020) or incorporated into a mixed medium with other ices (e.g., P. Ehrenfreund et al. 1999; S. Protopapa et al. 2024). Nevertheless, the broad agreement in overall CO_2 fundamental band shape between Charon and the other bright KBOs—including Salacia and Máni—may reflect similar underlying spectral profiles, suggesting that the same processes that drive the complex CO_2 spectral signature on Charon may be at play across the large-sized and midsized KBO population. Such a scenario could be confirmed through the analysis of higher-quality spectra derived from future observations, combined with additional laboratory investigations into the effects of thermal and radiation-driven processing on CO_2 ice.

4. Summary

We presented the JWST/NIRSpec spectra of the mid-sized KBOs Salacia and M \acute{a} ni. The two spectra show clear similarities, with prominent absorption bands of H $_2$ O and CO $_2$ ice. No additional features from CH $_4$, C $_2$ H $_6$, or other hydrocarbons were detected. A comparison with spectroscopic data of smaller objects in the trans-Neptunian region indicates that Salacia and M \acute{a} ni belong to the spectrally prominent water (H $_2$ O-type) KBO class. An ensemble analysis of H $_2$ O-type spectra revealed several salient trends within this population:

1. The band depth of the H $_2$ O-ice absorption feature at $3\,\mu\text{m}$ correlates strongly with object size, as inferred from the absolute magnitudes, with larger KBOs displaying deeper bands. This covariance suggests an overall increase in the relative surface abundance of H $_2$ O ice, although additional variability across the sample due to grain size differences may also contribute to the distribution of band depths.
2. While an analogous positive covariance between the measured $2\,\mu\text{m}$ H $_2$ O-ice band depths and target diameter is evident among the largest KBOs, this trend becomes less pronounced at smaller sizes. There is strong evidence for a bimodality in $2\,\mu\text{m}$ band depth among KBOs with $4 < H_V < 8$, suggesting systematic differences in H $_2$ O-ice grain size or vertical stratification among objects with similar sizes.
3. There is a marked transition in the strength of the $\sim 4.25\,\mu\text{m}$ CO $_2$ -ice absorption band at $H_V \sim 5 - 6$. Larger objects have systematically shallower CO $_2$ features, although the presence of selection biases within the spectroscopic sample with respect to the various KBO dynamical classes prevent us from making a definitive claim about the size-dependent nature of this apparent trend.
4. The shape of the $\sim 4.25\,\mu\text{m}$ CO $_2$ -ice feature also appears to vary with target size. While smaller objects have bands centered at $\sim 4.27\,\mu\text{m}$ that are consistent with pure crystalline CO $_2$ ice or H $_2$ O:CO $_2$ mixtures, the larger KBOs within our sample show broader features that extend to shorter wavelengths. The latter may be caused by additional contributions from either (1) irradiated and/or complexed CO $_2$, or (2) a thin veneer of CO $_2$ overlaying a reflective H $_2$ O-rich layer, as suggested by previous spectral modeling of Charon.

The trend between H $_2$ O-ice abundance and size provides tentative evidence for the emergent effects of internal heating and cryovolcanic activity on mid-sized KBOs such as Salacia and M \acute{a} ni, although follow-up investigations are needed to disentangle the effects of H $_2$ O-ice grain size and possible vertical stratification on the surfaces. Future work that synthesizes these results with new insights from studies of interior thermal evolution, investigations of endogenous and exogenous surface alteration, and detailed spectral modeling will greatly refine our understanding of the various physical and chemical processes that have sculpted the observed compositional diversity among water-ice-rich KBOs.

Acknowledgments

This work is based on observations made with the NASA/ESA/CSA James Webb Space Telescope. The data were obtained from the Mikulski Archive for Space Telescopes at the Space Telescope Science Institute, which is operated by the Association of Universities for Research in Astronomy, Inc., under NASA contract NAS 5-03127 for JWST. These observations are associated with Program #1191. The specific observations analyzed can be accessed via <https://doi.org/10.17909/252c-8q63>.

H.B.H. and S.N.M. acknowledge support from NASA JWST Interdisciplinary Scientist grant 21-SMDSS21-0013. R.B. acknowledges support from the CNES-France (JWST mission). N.P.-A. acknowledges funding through the ATRAE program of the Ministry of Science, Innovation, and Universities (MCIU) and the State Agency for Research (AEI) in Spain.

Facility: JWST/NIRSpec.

Software: `astropy` (Astropy Collaboration et al. 2013, 2018, 2022), `jwst` (H. Bushouse et al. 2025), `jwstspec` (I. Wong 2025), `matplotlib` (J. D. Hunter 2007), `numpy` (C. R. Harris et al. 2020), `scipy` (P. Virtanen et al. 2020).

References

- Armand, G. 1977, *SurSc*, 66, 321, doi: [10.1016/0039-6028\(77\)90414-9](https://doi.org/10.1016/0039-6028(77)90414-9)
- Astropy Collaboration, Robitaille, T. P., Tollerud, E. J., et al. 2013, *A&A*, 558, A33, doi: [10.1051/0004-6361/201322068](https://doi.org/10.1051/0004-6361/201322068)
- Astropy Collaboration, Price-Whelan, A. M., Sipőcz, B. M., et al. 2018, *AJ*, 156, 123, doi: [10.3847/1538-3881/aabc4f](https://doi.org/10.3847/1538-3881/aabc4f)
- Astropy Collaboration, Price-Whelan, A. M., Lim, P. L., et al. 2022, *ApJ*, 935, 167, doi: [10.3847/1538-4357/ac7c74](https://doi.org/10.3847/1538-4357/ac7c74)
- Barr, A. C., & Schwamb, M. E. 2016, *MNRAS*, 460, 1542, doi: [10.1093/mnras/stw1052](https://doi.org/10.1093/mnras/stw1052)
- Barucci, M. A., Alvarez-Candal, A., Merlin, F., et al. 2011, *Icar*, 214, 297, doi: [10.1016/j.icarus.2011.04.019](https://doi.org/10.1016/j.icarus.2011.04.019)
- Barucci, M. A., Brown, M. E., Emery, J. P., & Merlin, F. 2008, in *The Solar System Beyond Neptune*, ed. M. A. Barucci, H. Boehnhardt, D. P. Cruikshank, A. Morbidelli, & R. Dotson (Univ. Arizona Press), 143–160
- Belyakov, M., & Brown, M. E. 2025, *PSJ*, 6, 97, doi: [10.3847/PSJ/adc55d](https://doi.org/10.3847/PSJ/adc55d)
- Bennett, C. J., Jamieson, C. S., Osamura, Y., & Kaiser, R. I. 2006, *ApJ*, 653, 792, doi: [10.1086/508561](https://doi.org/10.1086/508561)
- Bernardinelli, P. H., Bernstein, G. M., Abbott, T. M. C., et al. 2025, *AJ*, 169, 305, doi: [10.3847/1538-3881/adc459](https://doi.org/10.3847/1538-3881/adc459)
- Bierson, C. J., & Nimmo, F. 2019, *Icar*, 326, 10, doi: [10.1016/j.icarus.2019.01.027](https://doi.org/10.1016/j.icarus.2019.01.027)
- Bockelée-Morvan, D., Lellouch, E., Poch, O., et al. 2024, *A&A*, 681, A27, doi: [10.1051/0004-6361/202347326](https://doi.org/10.1051/0004-6361/202347326)
- Bohlin, R. C., Gordon, K. D., & Tremblay, P. E. 2014, *PASP*, 126, 711, doi: [10.1086/677655](https://doi.org/10.1086/677655)
- Böker, T., Beck, T. L., Birkmann, S. M., et al. 2023, *PASP*, 135, 038001, doi: [10.1088/1538-3873/acb846](https://doi.org/10.1088/1538-3873/acb846)
- Brown, M. E. 2012, *AREPS*, 40, 467, doi: [10.1146/annurev-earth-042711-105352](https://doi.org/10.1146/annurev-earth-042711-105352)
- Brown, M. E., & Butler, B. J. 2017, *AJ*, 154, 19, doi: [10.3847/1538-3881/aa6346](https://doi.org/10.3847/1538-3881/aa6346)
- Brown, M. E., Schaller, E. L., & Fraser, W. C. 2011, *ApJL*, 739, L60, doi: [10.1088/2041-8205/739/2/L60](https://doi.org/10.1088/2041-8205/739/2/L60)
- Brown, M. E., Schaller, E. L., & Fraser, W. C. 2012, *AJ*, 143, 146, doi: [10.1088/0004-6256/143/6/146](https://doi.org/10.1088/0004-6256/143/6/146)

- Brunetto, R., Barucci, M. A., Dotto, E., & Strazzulla, G. 2006, *ApJ*, 644, 646, doi: [10.1086/503359](https://doi.org/10.1086/503359)
- Buratti, B. J., Hofgartner, J. D., Hicks, M. D., et al. 2017, *Icar*, 287, 207, doi: [10.1016/j.icarus.2016.11.012](https://doi.org/10.1016/j.icarus.2016.11.012)
- Bushouse, H., Eisenhamer, J., Dencheva, N., et al. 2025, JWST Calibration Pipeline, v1.17.1, Zenodo, doi: [10.5281/zenodo.6984365](https://doi.org/10.5281/zenodo.6984365)
- Cañas, M. H., Lyra, W., Carrera, D., et al. 2024, *PSJ*, 5, 55, doi: [10.3847/PSJ/ad1d5b](https://doi.org/10.3847/PSJ/ad1d5b)
- Cartwright, R. J., Villanueva, G. L., Holler, B. J., et al. 2024, *PSJ*, 5, 60, doi: [10.3847/PSJ/ad23e6](https://doi.org/10.3847/PSJ/ad23e6)
- Collyer, C., Fernandez-Valenzuela, E., Ortiz, J. L., et al. 2025, *arXiv e-prints*, arXiv:2509.02734, doi: [10.48550/arXiv.2509.02734](https://doi.org/10.48550/arXiv.2509.02734)
- Cook, J. C., Desch, S. J., Roush, T. L., Trujillo, C. A., & Geballe, T. R. 2007, *ApJ*, 663, 1406, doi: [10.1086/518222](https://doi.org/10.1086/518222)
- Cruikshank, D. P., Meyer, A. W., Brown, R. H., et al. 2010, *Icar*, 206, 561, doi: [10.1016/j.icarus.2009.07.012](https://doi.org/10.1016/j.icarus.2009.07.012)
- Dalle Ore, C. M., Barucci, M. A., Emery, J. P., et al. 2009, *A&A*, 501, 349, doi: [10.1051/0004-6361/200911752](https://doi.org/10.1051/0004-6361/200911752)
- De Prá, M. N., Hénault, E., Pinilla-Alonso, N., et al. 2025, *NatAs*, 9, 252, doi: [10.1038/s41550-024-02276-x](https://doi.org/10.1038/s41550-024-02276-x)
- Delsanti, A., Merlin, F., Guilbert-Lepoutre, A., et al. 2010, *A&A*, 520, A40, doi: [10.1051/0004-6361/201014296](https://doi.org/10.1051/0004-6361/201014296)
- Desch, S. J., Cook, J. C., Doggett, T. C., & Porter, S. B. 2009, *Icar*, 202, 694, doi: [10.1016/j.icarus.2009.03.009](https://doi.org/10.1016/j.icarus.2009.03.009)
- Ehrenfreund, P., Kerkhof, O., Schutte, W. A., et al. 1999, *A&A*, 350, 240
- Emery, J. P., Wong, I., Brunetto, R., et al. 2024, *Icar*, 414, 116017, doi: [10.1016/j.icarus.2024.116017](https://doi.org/10.1016/j.icarus.2024.116017)
- Fornasier, S., Lellouch, E., Müller, T., et al. 2013, *A&A*, 555, A15, doi: [10.1051/0004-6361/201321329](https://doi.org/10.1051/0004-6361/201321329)
- Gerakines, P. A., & Hudson, R. L. 2020, *ApJ*, 901, 52, doi: [10.3847/1538-4357/abad39](https://doi.org/10.3847/1538-4357/abad39)
- Gerakines, P. A., Moore, M. H., & Hudson, R. L. 2001, *JGR*, 106, 33381, doi: [10.1029/2000JE001320](https://doi.org/10.1029/2000JE001320)
- Glein, C. R., Grundy, W. M., Lunine, J. I., et al. 2024, *Icar*, 412, 115999, doi: [10.1016/j.icarus.2024.115999](https://doi.org/10.1016/j.icarus.2024.115999)
- Grundy, W. M., Noll, K. S., Buie, M. W., et al. 2019a, *Icar*, 334, 30, doi: [10.1016/j.icarus.2018.12.037](https://doi.org/10.1016/j.icarus.2018.12.037)
- Grundy, W. M., & Schmitt, B. 1998, *JGR*, 103, 25809, doi: [10.1029/98JE00738](https://doi.org/10.1029/98JE00738)
- Grundy, W. M., Cruikshank, D. P., Gladstone, G. R., et al. 2016, *Natur*, 539, 65, doi: [10.1038/nature19340](https://doi.org/10.1038/nature19340)
- Grundy, W. M., Noll, K. S., Roe, H. G., et al. 2019b, *Icar*, 334, 62, doi: [10.1016/j.icarus.2019.03.035](https://doi.org/10.1016/j.icarus.2019.03.035)
- Grundy, W. M., Wong, I., Glein, C. R., et al. 2024, *Icar*, 411, 115923, doi: [10.1016/j.icarus.2023.115923](https://doi.org/10.1016/j.icarus.2023.115923)
- Guilbert-Lepoutre, A., Prialnik, D., & Métayer, R. 2020, in *The Trans-Neptunian Solar System*, ed. D. Prialnik, M. A. Barucci, & L. Young (Elsevier), 183–201, doi: [10.1016/B978-0-12-816490-7.00008-4](https://doi.org/10.1016/B978-0-12-816490-7.00008-4)
- Hansen, G. B., & McCord, T. B. 2004, *JGRE*, 109, E01012, doi: [10.1029/2003JE002149](https://doi.org/10.1029/2003JE002149)
- Harris, C. R., Millman, K. J., van der Walt, S. J., et al. 2020, *Natur*, 585, 357, doi: [10.1038/s41586-020-2649-2](https://doi.org/10.1038/s41586-020-2649-2)
- Hartigan, J. A., & Hartigan, P. M. 1985, *AnSta*, 13, 70, doi: [10.1214/aos/1176346577](https://doi.org/10.1214/aos/1176346577)
- He, J., Emtiaz, S., Boogert, A., & Vidali, G. 2018, *ApJ*, 869, 41, doi: [10.3847/1538-4357/aae9dc](https://doi.org/10.3847/1538-4357/aae9dc)
- Hibbitts, C. A., McCord, T. B., & Hansen, G. B. 2000, *JGR*, 105, 22541, doi: [10.1029/1999JE001101](https://doi.org/10.1029/1999JE001101)
- Hibbitts, C. A., Pappalardo, R. T., Hansen, G. B., & McCord, T. B. 2003, *JGRE*, 108, 5036, doi: [10.1029/2002JE001956](https://doi.org/10.1029/2002JE001956)
- Holler, B. J., Brunetto, R., Cruikshank, D. P., et al. 2025, *RNAAS*, 9, 241, doi: [10.3847/2515-5172/ae03a2](https://doi.org/10.3847/2515-5172/ae03a2)
- Hunter, J. D. 2007, *CSE*, 9, 90, doi: [10.1109/MCSE.2007.55](https://doi.org/10.1109/MCSE.2007.55)
- Husmann, H., Sohl, F., & Spohn, T. 2006, *Icar*, 185, 258, doi: [10.1016/j.icarus.2006.06.005](https://doi.org/10.1016/j.icarus.2006.06.005)
- Jakobsen, P., Ferruit, P., Alves de Oliveira, C., et al. 2022, *A&A*, 661, A80, doi: [10.1051/0004-6361/202142663](https://doi.org/10.1051/0004-6361/202142663)
- Jones, B. M., Kaiser, R. I., & Strazzulla, G. 2014, *ApJ*, 788, 170, doi: [10.1088/0004-637X/788/2/170](https://doi.org/10.1088/0004-637X/788/2/170)
- Kiss, C., Marton, G., Parker, A. H., et al. 2019, *Icar*, 334, 3, doi: [10.1016/j.icarus.2019.03.013](https://doi.org/10.1016/j.icarus.2019.03.013)
- Levison, H. F., Morbidelli, A., Van Laerhoven, C., Gomes, R., & Tsiganis, K. 2008, *Icar*, 196, 258, doi: [10.1016/j.icarus.2007.11.035](https://doi.org/10.1016/j.icarus.2007.11.035)
- Licandro, J., Pinilla-Alonso, N., Holler, B. J., et al. 2025, *NatAs*, 9, 245, doi: [10.1038/s41550-024-02417-2](https://doi.org/10.1038/s41550-024-02417-2)
- Lisse, C. M., Young, L. A., Cruikshank, D. P., et al. 2021, *Icar*, 356, 114072, doi: [10.1016/j.icarus.2020.114072](https://doi.org/10.1016/j.icarus.2020.114072)
- Malamud, U., & Prialnik, D. 2015, *Icar*, 246, 21, doi: [10.1016/j.icarus.2014.02.027](https://doi.org/10.1016/j.icarus.2014.02.027)
- Markwardt, L., Wen Lin, H., Holler, B. J., et al. 2025, *PSJ*, 6, 154, doi: [10.3847/PSJ/addec4](https://doi.org/10.3847/PSJ/addec4)
- Mastrapa, R. M., Sandford, S. A., Roush, T. L., Cruikshank, D. P., & Dalle Ore, C. M. 2009, *ApJ*, 701, 1347, doi: [10.1088/0004-637X/701/2/1347](https://doi.org/10.1088/0004-637X/701/2/1347)
- Mastrapa, R. M. E., Grundy, W. M., & Gudipati, M. S. 2013, *ASSL*, 356, 371, doi: [10.1007/978-1-4614-3076-6_11](https://doi.org/10.1007/978-1-4614-3076-6_11)
- McKinnon, W. B., Prialnik, D., Stern, S. A., & Coradini, A. 2008, in *The Solar System Beyond Neptune*, ed. M. A. Barucci, H. Boehnhardt, D. P. Cruikshank, A. Morbidelli, & R. Dotson (Univ. Arizona Press), 213–241
- McKinnon, W. B., Stern, S. A., Weaver, H. A., et al. 2017, *Icar*, 287, 2, doi: [10.1016/j.icarus.2016.11.019](https://doi.org/10.1016/j.icarus.2016.11.019)
- Menten, S. M., Sori, M. M., & Bramson, A. M. 2022, *NatCo*, 13, 4457, doi: [10.1038/s41467-022-31846-8](https://doi.org/10.1038/s41467-022-31846-8)
- Moore, J. M., & McKinnon, W. B. 2021, *AREPS*, 49, doi: [10.1146/annurev-earth-071720-051448](https://doi.org/10.1146/annurev-earth-071720-051448)
- Moroz, L., Baratta, G., Strazzulla, G., et al. 2004, *Icar*, 170, 214, doi: [10.1016/j.icarus.2004.02.003](https://doi.org/10.1016/j.icarus.2004.02.003)
- Moseley, S. H., Arendt, R. G., Fixsen, D. J., et al. 2010, *SPIE*, 7742, 77421B, doi: [10.1117/12.866773](https://doi.org/10.1117/12.866773)
- Müller, T., Lellouch, E., & Fornasier, S. 2020, in *The Trans-Neptunian Solar System*, ed. D. Prialnik, M. A. Barucci, & L. Young (Elsevier), 153–181, doi: [10.1016/B978-0-12-816490-7.00007-2](https://doi.org/10.1016/B978-0-12-816490-7.00007-2)
- Nesvorný, D. 2018, *ARA&A*, 56, 137, doi: [10.1146/annurev-astro-081817-052028](https://doi.org/10.1146/annurev-astro-081817-052028)
- Nesvorný, D., Vokrouhlický, D., & Fraser, W. C. 2022, *AJ*, 163, 137, doi: [10.3847/1538-3881/ac4bc9](https://doi.org/10.3847/1538-3881/ac4bc9)
- Noll, K. S., Grundy, W. M., Chiang, E. I., Margot, J. L., & Kern, S. D. 2008, in *The Solar System Beyond Neptune*, ed. M. A. Barucci, H. Boehnhardt, D. P. Cruikshank, A. Morbidelli, & R. Dotson (Univ. Arizona Press), 345–363, doi: [10.48550/arXiv.astro-ph/0703134](https://doi.org/10.48550/arXiv.astro-ph/0703134)
- Noll, K. S., Levison, H. F., Stephens, D. C., & Grundy, W. M. 2006, *IAUC*, 8751, 1
- Pál, A., Kiss, C., Müller, T. G., et al. 2012, *A&A*, 541, L6, doi: [10.1051/0004-6361/201218874](https://doi.org/10.1051/0004-6361/201218874)
- Pike, R. E., Fraser, W. C., Schwamb, M. E., et al. 2017, *AJ*, 154, 101, doi: [10.3847/1538-3881/aa83b1](https://doi.org/10.3847/1538-3881/aa83b1)
- Pinilla-Alonso, N., Licandro, J., & Lorenzi, V. 2008, *A&A*, 489, 455, doi: [10.1051/0004-6361/200810226](https://doi.org/10.1051/0004-6361/200810226)
- Pinilla-Alonso, N., Roush, T. L., Marzo, G. A., Cruikshank, D. P., & Dalle Ore, C. M. 2011, *Icar*, 215, 75, doi: [10.1016/j.icarus.2011.07.004](https://doi.org/10.1016/j.icarus.2011.07.004)
- Pinilla-Alonso, N., Brunetto, R., De Prá, M. N., et al. 2025, *NatAs*, 9, 230, doi: [10.1038/s41550-024-02433-2](https://doi.org/10.1038/s41550-024-02433-2)
- Protopapa, S., Cook, J. C., Grundy, W. M., et al. 2021, in *The Pluto System After New Horizons*, ed. S. A. Stern, J. M. Moore, W. M. Grundy, L. A. Young, & R. P. Binzel (Univ. Arizona Press), 433–456, doi: [10.2458/azu_uapress_9780816540945-ch019](https://doi.org/10.2458/azu_uapress_9780816540945-ch019)
- Protopapa, S., Sunshine, J. M., Feaga, L. M., et al. 2014, *Icar*, 238, 191, doi: [10.1016/j.icarus.2014.04.008](https://doi.org/10.1016/j.icarus.2014.04.008)
- Protopapa, S., Raut, U., Wong, I., et al. 2024, *NatCo*, 15, 8247, doi: [10.1038/s41467-024-51826-4](https://doi.org/10.1038/s41467-024-51826-4)
- Protopapa, S., Wong, I., Lellouch, E., et al. 2025, *ApJL*, 991, L34, doi: [10.3847/2041-8213/adfe63](https://doi.org/10.3847/2041-8213/adfe63)

- Proudfoot, B., Grundy, W., Ragozzine, D., & Fernández-Valenzuela, E. 2025, arXiv e-prints, arXiv:2511.07351, doi: [10.48550/arXiv.2511.07351](https://doi.org/10.48550/arXiv.2511.07351)
- Quirico, E., Bacmann, A., Wolters, C., et al. 2023, *Icar*, 394, 115396, doi: [10.1016/j.icarus.2022.115396](https://doi.org/10.1016/j.icarus.2022.115396)
- Rauscher, B. J., Arendt, R. G., Fixsen, D. J., et al. 2012, *SPIE*, 8453, 84531F, doi: [10.1117/12.926089](https://doi.org/10.1117/12.926089)
- Raut, U., & Baragiola, R. A. 2013, *ApJ*, 772, 53, doi: [10.1088/0004-637X/772/1/53](https://doi.org/10.1088/0004-637X/772/1/53)
- Raut, U., Teolis, B. D., Kammer, J. A., et al. 2022, *SciA*, 8, eabq5701, doi: [10.1126/sciadv.abq5701](https://doi.org/10.1126/sciadv.abq5701)
- Roe, H. G., Brown, M. E., Barkume, K. M., & Marsden, B. G. 2005, *MPEC*, 2005-J26
- Rommel, F. L., Braga-Ribas, F., Ortiz, J. L., et al. 2023, *A&A*, 678, A167, doi: [10.1051/0004-6361/202346892](https://doi.org/10.1051/0004-6361/202346892)
- Schaller, E. L., & Brown, M. E. 2007a, *ApJL*, 659, L61, doi: [10.1086/516709](https://doi.org/10.1086/516709)
- Schaller, E. L., & Brown, M. E. 2007b, *ApJL*, 670, L49, doi: [10.1086/524140](https://doi.org/10.1086/524140)
- Schaller, E. L., & Brown, M. E. 2008, *ApJL*, 684, L107, doi: [10.1086/592232](https://doi.org/10.1086/592232)
- Schiltz, L., Escribano, B., Muñoz Caro, G. M., et al. 2024, *A&A*, 688, A155, doi: [10.1051/0004-6361/202449846](https://doi.org/10.1051/0004-6361/202449846)
- Sharkey, B. N. L., Rivkin, A. S., Cartwright, R. J., et al. 2025, *PSJ*, 6, 242, doi: [10.3847/PSJ/ae04dd](https://doi.org/10.3847/PSJ/ae04dd)
- Stansberry, J. A., Grundy, W. M., Mueller, M., et al. 2012, *Icar*, 219, 676, doi: [10.1016/j.icarus.2012.03.029](https://doi.org/10.1016/j.icarus.2012.03.029)
- Steckloff, J. K., Lisse, C. M., Safrit, T. K., et al. 2021, *Icar*, 356, 113998, doi: [10.1016/j.icarus.2020.113998](https://doi.org/10.1016/j.icarus.2020.113998)
- Tegler, S. C., Romanishin, W., & Consolmagno, G. J. 2016, *AJ*, 152, 210, doi: [10.3847/0004-6256/152/6/210](https://doi.org/10.3847/0004-6256/152/6/210)
- Trujillo, C. A., Brown, M. E., Helin, E. F., et al. 2002, *MPEC*, 2002-W27
- Trumbo, S. K., & Brown, M. E. 2023, *Sci*, 381, 1308, doi: [10.1126/science.adg4155](https://doi.org/10.1126/science.adg4155)
- Vilenius, E., Kiss, C., Mommert, M., et al. 2012, *A&A*, 541, A94, doi: [10.1051/0004-6361/201118743](https://doi.org/10.1051/0004-6361/201118743)
- Villanueva, G. L., Smith, M. D., Protopapa, S., Faggi, S., & Mandell, A. M. 2018, *JQSRT*, 217, 86, doi: [10.1016/j.jqsrt.2018.05.023](https://doi.org/10.1016/j.jqsrt.2018.05.023)
- Villanueva, G. L., Hammel, H. B., Milam, S. N., et al. 2023, *Sci*, 381, 1305, doi: [10.1126/science.adg4270](https://doi.org/10.1126/science.adg4270)
- Virtanen, P., Gommers, R., Oliphant, T. E., et al. 2020, *NatMe*, 17, 261, doi: [10.1038/s41592-019-0686-2](https://doi.org/10.1038/s41592-019-0686-2)
- Volk, K., & Van Laerhoven, C. 2024, *RNAAS*, 8, 36, doi: [10.3847/2515-5172/ad22d4](https://doi.org/10.3847/2515-5172/ad22d4)
- Warren, S. G., & Brandt, R. E. 2008, *JGRD*, 113, D14220, doi: [10.1029/2007JD009744](https://doi.org/10.1029/2007JD009744)
- Wong, I. 2025, *jwstspec*, v0.6, Zenodo, doi: [10.5281/zenodo.17186395](https://doi.org/10.5281/zenodo.17186395)
- Wong, I., & Brown, M. E. 2016, *AJ*, 152, 90, doi: [10.3847/0004-6256/152/4/90](https://doi.org/10.3847/0004-6256/152/4/90)
- Wong, I., & Brown, M. E. 2017, *AJ*, 153, 145, doi: [10.3847/1538-3881/aa60c3](https://doi.org/10.3847/1538-3881/aa60c3)
- Wong, I., Holler, B. J., Fraser, W. C., & Brown, M. E. 2025, *PSJ*, 6, 271, doi: [10.3847/PSJ/ae1d73](https://doi.org/10.3847/PSJ/ae1d73)
- Wong, I., Brown, M. E., Emery, J. P., et al. 2024, *PSJ*, 5, 87, doi: [10.3847/PSJ/ad2fc3](https://doi.org/10.3847/PSJ/ad2fc3)
- Zhang, C., Zhu, C., Turner, A. M., et al. 2023, *SciA*, 9, eadg6936, doi: [10.1126/sciadv.adg6936](https://doi.org/10.1126/sciadv.adg6936)